JOURNAL OF GEOPHYSICAL RESEARCH, VOL. 103, NO. C4, PAGES 7901–7915, APRIL 15, 1998

The effect of assimilating ERS-1 fast delivery wave data into the North Atlantic WAM model

E. M. Dunlap,[1] R. B. Olsen,[2] L. Wilson,[3] S. De Margerie,[1] and R. Lalbeharry[3]

Abstract. The launch of the European ERS satellites has provided a new source of wave information that is particularly suitable for use in improving wave forecasts in the open ocean. We have implemented and tested a simple system for assimilating corrections to model wave fields produced by the WAM model, where the corrections are derived from inverted synthetic aperture radar (SAR) image spectra from ERS-1. Corrections are applied to significant wave height, mean period and direction for wave modes that are detectable in both the model and the SAR data. The system has been tested in a storm situation and in moderate conditions using buoy data and altimeter data, as well as SAR observations for verification. Overall, it is demonstrated that the net effect of assimilating SAR data is beneficial but very small. The small impact is due at least partly to relatively small spatial and temporal coverage of the SAR wave mode data. Locally larger impacts were found in the storm situation in individual cases where SAR observations were collocated with independent buoy observations.

1. Introduction

Up until a few years ago, ocean wave models were run without the use of any wave observations. Model simulations of wave growth, propagation, and decay were obtained using marine winds as input, either as a series of analyses ("hindcast mode") or as forecast winds from an atmospheric model ("forecast mode"). Wave observations were not used for two reasons. First, wave models have been shown to simulate the wave field quite well if they are driven by a consistent high-quality wind field [*Graber et al.*, 1994]. Second, so few wave observations were available that they could not be expected to have a significant impact on regional or ocean basin scale wave simulations. With the launch of ERS-1 in July 1991 the spatial and temporal coverage of wave observations increased dramatically, making their use to initialize wave models operationally practical. ERS-1 (and recently ERS-2) wave observations are available in two forms, wave heights from the radar altimeter, and estimates of the two-dimensional (2-D) wave spectrum from the active microwave instrument (AMI) operating in synthetic aperture radar (SAR) mode. The latter offers the opportunity of obtaining real-time wave observations that are the most complete and consistent with the output of a wave model, an estimate of the two-dimensional spectral wave energy.

The general purpose of data assimilation is to change a model's estimate of the state of its geophysical variables toward their true state, using information obtained from observations. Both model and data are assumed to contain errors, which must be accounted for in the assimilation procedure. With remotely sensed observations it is often the case that the geophysical variable is not directly observed; its values must be inferred or estimated. The raw SAR mode data from ERS-1 are in the form of radar backscatter measurements. The 2-D SAR image spectra estimated from analysis of spatial patterns in the SAR image intensities are known to be a representation of the corresponding ocean wave spectra, subject to certain limitations. *Hasselmann and Hasselmann* [1991] (hereinafter referred to as HH) were the first to propose a practical and robust scheme for translating SAR spectra into ocean wave spectra. The HH algorithm accounts for the limitations of the SAR spectrum and produces a SAR enhanced estimate of the ocean spectrum by systematically combining the SAR information with estimates of the ocean spectrum from a wave model. The wave model can be expected to provide a full spectrum that is spatially consistent and consistent with the physics of wave growth, propagation, and decay, while the SAR spectrum can be used to correct for errors in the model simulation due, for example, to inaccuracies in the input wind field. The HH algorithm has been run through many thousands of ERS-1 SAR images and has been shown to function reliably [*Brüning et al.*, 1994a].

The HH algorithm provides an estimate of the ocean spectrum from SAR data at the SAR observation location. The process of data assimilation also must include a systematic means of correcting the model wave spectra at all locations within a reasonable range of influence of the observation site. Two-dimensional interpolation methods have been in use in meteorological applications for many years. For example, Cressman-type methods [*Cressman*, 1959] are the simplest and involve simple interpolation of the differences between model estimates ("first guess") and the observations to nearby grid points using a weighting function that is inversely related to the distance of the observation site from the grid point. If the weights are determined using the error statistics of the model and their spatial correlation, the method is known as optimum interpolation [*Gandin*, 1963]. Collectively, these methods are referred to as sequential insertion methods, since the strategy is to run the model forward in time, stopping at regular intervals to assimilate data that are available and all valid at about the same time, then continuing the model run with the corrected model state.

[1]ASA Consulting Ltd., Halifax, Nova Scotia, Canada.
[2]Satlantic, Inc., Halifax, Nova Scotia, Canada.
[3]Atmospheric Environment Service, Environment Canada, Dorval, Quebec.

Paper number 97JC02570.
0148-0227/98/97JC-02570$09.00

Data assimilation methods used so far in wave modeling are of the sequential insertion type and have been applied mostly to altimeter data. Examples are the assimilation of Seasat altimeter wave heights into the U.K. Meteorological Office global wave model [*Francis and Stratton*, 1990] and the assimilation of altimeter wave heights into the wave model WAM [*Lionello et al.*, 1992]. Ideally, one would like to combine the algorithm that matches the first guess and observation at the observation point with the assimilation step, which spreads the corrections spatially. In meteorological applications this is now being accomplished by 3-D variational methods [e.g., *Talagrand and Courtier*, 1987]. The variational approach is being pursued actively in operational meteorological data assimilation applications in many national weather centers, but its application in wave data assimilation is so far limited to tests with idealized data (see for example, *de las Heras and Janssen* [1992]). Variational assimilation will probably be the optimal methodology in wave assimilation as well, but it is more computationally demanding than the older methods. We have thus opted for this first wave data assimilation system to adopt a step-by-step approach, to use methods which had already been tested in wave applications before embarking on experiments with new methods applied to a new data source.

Our goal was to develop a data assimilation system that would be sophisticated enough to give an initial assessment of the impact of SAR wave data on analyses and forecasts from the WAM model. To accomplish this, we put together a full assimilation system by adapting simple assimilation methods and tested it on a variety of North Atlantic cases, including both specific extreme storms and nonstorm situations. The results of these tests are described in this paper. First, the design and construction of the assimilation procedure is described; then results are shown for one storm case, the "Storm of the Century," and for a 1-month period of regular wave forecasts.

2. Assimilation System

Our assimilation system consists of three main components: the wave model WAM, the SAR data preprocessor, and the assimilation module. The assimilation module consists of two main subcomponents: SAR inversion at observation points and interpolation of SAR-induced corrections within the model grid domain. The following sections describe all these components.

2.1. WAM

In this study we have used the wave model WAM, described by the *WAMDI Group* [1988] with a coupling to the atmospheric boundary layer following *Janssen* [1991]. This version of WAM, referred to as Cycle-4, was implemented on a 1.0° × 1.0° latitude-longitude grid that covers the northwest Atlantic extending from 25°N to 70°N and from 80°W to 15°W and includes 2318 water points. The model simulates the 2-D spectrum of wave energy discretised into 24 directional bands, 15° wide, and 25 frequency bands logarithmically spaced from 0.042 Hz to 0.41 Hz with an increment-to-frequency ratio equal to 0.1.

2.2. SAR Data Processing

The ERS-1 and 2 satellites carry the active microwave instrument package as their main payload. In the SAR wave mode the AMI acquires signal data to produce a SAR image (imagette) every 200 km along track. Each imagette is nominally 5 km × 5 km. The across-track position of the imagette is programmed by the European Space Agency (ESA) within the 100-km SAR image mode swath. The imagettes are subsequently transformed into image spectra using a fast Fourier transform (FFT)–based approach. The spectral calculations are performed on intensity images (amplitude squared) where the mean value has been subtracted. For a more detailed description, see *Brooker* [1994]. A Hamming window is applied to the data prior to the FFT, and the data are subsequently zero-padded to a sample size of 512 × 512 values before applying the Fourier transform. The resulting spectrum in Cartesian coordinates is converted to polar coordinates on a scale that is logarithmic in wave length, sampled at 12 wavelengths, and specified in 12 directions between 0° and 180°, rescaled to eight bits on a linear scale. The sampling is designed to match the typical spectral representation used in global wave forecast models such as WAM. The spectra are also filtered to wavelength limits of 100 m to 1000 m. The data are subsequently transmitted to ESA/European Space Research Institute (ESRIN) for compilation of global data sets and redistributed to national users. In Canada the data are received at the Atmospheric Environment Service (AES), where they are decoded and converted into a format suitable for ingestion into the Assimilating WAM model, AWAM. During the conversion process, the data are sorted and divided into files, each containing 3 hours worth of data, centered on each WAM model time step. This procedure also filters out data from outside the model domain.

2.3. Inversion

In order to extract ocean wave information from SAR wave data, the mechanisms by which SAR images ocean surface waves must be known. These mechanisms have been discussed extensively in the literature [e.g., *Jain*, 1981; *Alpers*, 1983; *Hasselmann et al.*, 1985; *Alpers and Brüning*, 1986; *Hasselmann and Alpers*, 1986; *Brüning et al.*, 1990, 1994b; *Jacobsen and Høgda*, 1994]. The predominant backscattering mechanism at incidence angles encountered with a spaceborne SAR is attributed to Bragg resonant scattering from short surface ripples [*Hasselmann et al.*, 1985]. This backscattering is modulated by three major processes, which contribute to long wave imaging: tilt modulation, hydrodynamic modulation and velocity bunching. The first two are related to the occurrence and local imaging geometry of scattering elements on the ocean surface which vary across the larger ocean waves. Wave orbital motion results in a shift of the backscattering elements, "bunching" them in the SAR image to form wave patterns. This is an effect that is specific to coherent imaging systems such as SAR. The relative importance of the modulation mechanisms is dependent on the propagation direction of the ocean surface gravity waves relative to the radar look direction, the sea state, the viewing geometry, and the satellite height and velocity. The velocity-bunching effect is proportional to the gradient of the radial orbital wave velocity in the azimuth direction.

One of the main limitations of SAR wave data results from the fact that the velocity-bunching effect is nonlinear [*Hasselmann et al.*, 1985], which causes rotation of the spectra toward the range direction and stretching [*Brüning et al.*, 1990]. Another limitation is the incompleteness of the ocean wave information contained in SAR image data. Loss of scene coherence due to orbital motion and the limited lifetime of the scattering elements leads to a loss of resolution in the azimuth direction [*Vachon et al.*, 1989, 1993], resulting in a scene-dependent loss of SAR imaging capability in the higher-azimuth wave numbers. SAR spectra therefore typically exhibit a cutoff in energy along the azimuth wave number axis that is dependent on sea state and wind speed. Furthermore, the ERS-1 SAR wave mode spectra are generated from single frames of imagery, producing a 180° ambiguity in the wave direction.

In the present approach we use the pure nondispersive velocity-bunching theory. The extension to a dispersive case is rather straightforward [*Krogstad et al.*, 1994]; however, it would introduce an additional azimuth spectral cutoff factor and is neglected for simplicity of calculation. The scanning distortion due to the motion of the surface during the scanning, which may be significant for airborne SAR [*Krogstad et al.*, 1994; *Krogstad*, 1992; *Raney and Lowry*, 1978] is negligible for satellite-borne SAR and is therefore neglected.

The HH SAR spectral inversion technique, which takes into account the limitations inherent in SAR wave data, is now a well-established procedure [HH; *Krogstad*, 1992; *Bao et al.*, 1994; *Brüning and Hasselmann*, 1993; *Brüning et al.*, 1994b; *Engen et al.*, 1994; *Hasselmann et al.*, 1996] and will not be described in detail here. In summary, the inverted SAR spectrum is obtained by a process of optimization based on the nonlinear transform from the ocean wave spectrum to the SAR image spectrum. This transform expresses the nonlinear effects of velocity bunching as a closed form integral. The a priori estimate of the wave spectrum (which is necessary to provide the information missing in SAR data) is supplied by a wave model, in our case WAM.

The nonlinear relationship between the image spectrum S_{SAR} and the ocean surface wave spectrum S_{wave} may be expressed generically as

$$S_{\mathrm{SAR}} = M_{\mathrm{nl}}(S_{\mathrm{wave}}) \tag{1}$$

Because of the limitations described above, this is not a one-to-one mapping.

The inversion scheme is based on the cost function and weighting functions defined as follows:

$$J = \sum_{\alpha=\mathrm{SAR,wave}} \int_{\mathbf{k}} (S_\alpha(\mathbf{k}) - S_\alpha^0)^2 W_\alpha(\mathbf{k})\, d\mathbf{k} \tag{2}$$

with the relative weights defined following HH. The shape of the data weight function $W_{\mathrm{SAR}}(\mathbf{k}) = S^0_{\mathrm{SAR}}(\mathbf{k})$ was selected to suppress the noise part of the observed SAR spectrum S^0_{SAR}, while the main role of the weight $W_{\mathrm{wave}}(\mathbf{k}) = \mu(B + \min(S_{\mathrm{wave}}(\mathbf{k}), S^0_{\mathrm{wave}}(\mathbf{k})))^{-1}$ is to remove the 180° ambiguity in the SAR image spectrum. The term in the cost function measuring the distance between the simulated and observed SAR spectrum gives identical values for the spectral components at the locations $\mathbf{k}$ and $-\mathbf{k}$. However, the term measuring the distance between the fitted wave spectrum and first-guess spectrum will give very large values to low energy spectral components and will favor the wave component at the peak location. The role of a small constant B is to avoid numerical infinity when the spectrum vanishes. The constant $\mu = 10^{-3} \max((S^0_{\mathrm{SAR}})^3)$ gives a low relative weight to the first-guess term in the cost function J, and also assures the dimensionless form of J. Other choices of weight functions used to control relative weighting of terms in the cost function are also possible [*Engen et al.*, 1994; *Krogstad et al.*, 1994; *Lasnier et al.*, 1994].

The SAR inversion algorithm described above results in a spectrum that combines information from the SAR, within the wave number band it is capable of sensing, and information from the first-guess wave spectrum. The end result of the inversion procedure in some cases leads to nonphysical discontinuities in the transition zone between the SAR capable wave number band and high wave numbers. The proposed remedy for this problem [*Hasselmann et al.*, 1996] implies additional adjustments of the first-guess wave systems at each inversion step, which requires additional computer time and was not implemented here.

2.4. Assimilation

The assimilation is carried out using a simple two-step scheme [*Hasselmann et al.*, 1994; *Komen et al.*, 1994] in which the corrections introduced by SAR wave data are first computed at the observation location and then spread over the model grid domain within a prescribed range of influence for the data. All SAR wave data available in a time window of 3 hours are assimilated simultaneously.

In order to reduce the dimensionality of the assimilation problem, and to make it practically feasible in an operational system, the corrections of only a small number of spectral parameters characterizing the main wave systems in each spectrum were assimilated. To accomplish this, spectral modes were identified in the SAR-derived wave spectra, and in WAM spectra at the grid points within the range of influence of each SAR spectrum location. For each mode the mean energy $\langle E \rangle$, mean frequency $\langle f \rangle$, and mean direction $\langle \theta \rangle$ were calculated. The mode separation algorithm used here was first proposed by *Gerling* [1992] and was described in detail by *Bauer et al.* [1995], *Hasselmann et al.* [1994], *Komen et al.* [1994, chapter V.4.3], and *Brüning et al.* [1994a].

Secondary partitions resulting from less significant peaks in the spectrum, characterized for example by relatively close peak locations or insufficiently deep valleys between partitions, were merged together. Also, all wind-sea partitions were combined into a single wind-sea mode, associated with the local wind forcing. Corresponding wave systems were subsequently identified for each SAR-extracted spectrum and the WAM spectra in its range of influence, using the approach of *Hasselmann et al.* [1994, 1996]. Modeled wave systems that could be correlated with SAR-derived wave systems were corrected, while SAR-derived wave systems that did not correspond to any of the modeled wave systems were simply added to the first-guess spectrum. Once the three spectral parameters were computed and matched for each distinct wave system, differences between the SAR-based estimates and model estimates were spread to neighboring grid points of the model.

The observed and corresponding modeled parameters were spread over a region of neighboring model grid points using a weighting function and a single-pass version of Cressman's approach [see *Cressman*, 1959; *Francis and Stratton*, 1990]. We define the spreading function as

$$P^{\mathrm{new}}(\mathbf{r}_j) = P^{\mathrm{WAM}}(\mathbf{r}_j) + \frac{\sum_{k=1}^{N_{\mathrm{obs}}} \varepsilon^2 w(\mathbf{r}_j - \mathbf{r}_k)(P^{\mathrm{obs}}(\mathbf{r}_k) - P^{\mathrm{WAM}}(\mathbf{r}_k))}{\sum_{k=1}^{N_{\mathrm{obs}}} \varepsilon^2 w(\mathbf{r}_j - \mathbf{r}_k) + 1} \tag{3}$$

Table 1. Dates for Case Studies

Case Study	Data Set	Period
1	Storm of the Century	March 11–21, 1993
2	Near real time	March 16 to April 16, 1996

where the weights $w(|\mathbf{r}_j - \mathbf{r}_k|)$ are a function only of the relative distance between the model and observation locations and where $\varepsilon^2 = \langle \varepsilon^2_{\mathrm{WAM}} \rangle / \langle \varepsilon^2_{\mathrm{obs}} \rangle$ is the expected model error variance, normalized by the expected observation error variance. The observation errors are assumed to be uncorrelated. At present, we assume $\varepsilon^2 = 1$ and use a simple functional form for the weights $w(|\mathbf{r}_j - \mathbf{r}_k|)$:

$$\begin{aligned} w(|\mathbf{r}_j - \mathbf{r}_k|) &= \exp(-R_{jk}) \approx 1 - R_{jk} \qquad R \le 1 \\ w(|\mathbf{r}_j - \mathbf{r}_k|) &= \exp(-R_{jk}) = 0 \qquad R > 1 \end{aligned} \tag{4}$$

where R is a dimensionless distance, computed in a spherical coordinate system as follows:

$$R = \sqrt{\frac{1}{2}\left(\frac{\Phi^2_{jk}}{L^2_{\mathrm{lat}}} + \frac{\Theta^2_{jk}}{L^2_{\mathrm{long}}}\right)} \tag{5}$$

The distances in the latitude and longitude direction (Φ_{jk} and Θ_{jk}, respectively) between observation and model grid points are normalized by the corresponding scales of the region of influence, L_{lat} and L_{long}. A linear weighting function is used here mainly for efficiency. It may be argued that a single correction pass, as compared with the optimal interpolation scheme [*Lionello et al.*, 1995], results in cases where areas with a high density of observations are given too much weight relative to observations in areas of low data density. This is not likely to be important in our case, however, as the SAR spectra are spaced evenly along the track and are spaced quite sparsely across the satellite tracks. We also note that this interpolation method is not strictly optimal, as we do not have available statistics for model and observation errors. The resulting estimate of the ocean surface wave field is therefore not optimized.

In principle, at least two distinct correlation length scales for wind sea and swell should be used. The wind sea correlation length scales correspond roughly to the storm generation area where the winds are strong, and would be of the order of 200 km. Correlation length scales of the order of 1000 km were used in assimilating altimeter data [*Lionello et al.*, 1992, 1995; *Bauer et al.*, 1992] in order to spread corrections to all grid points lying between satellite orbits. Here a moderate correlation length scale corresponding to five model grid points (about 500 km) was used. This represents not only a compromise of the two length scales above, but also a typical propagation distance for wave energy in a 3-hour time step at wavelengths dominated by swell. Analyzed wave spectra were constructed by topologically adjusting (scaling, stretching and rotating) each of the partitioned WAM wave systems to match its spectral parameters with the interpolated ones.

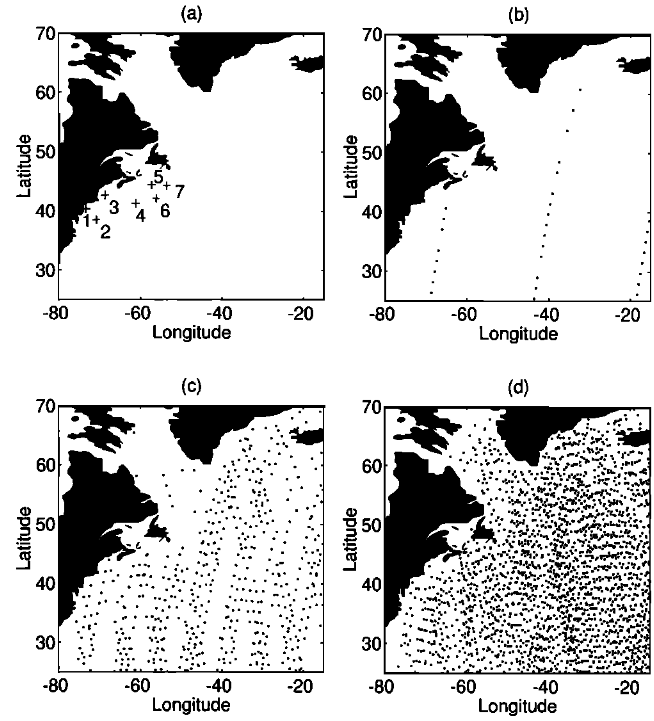

Figure 1. (a) Buoy locations used in verification, and coverage of the input ERS-1 SAR wave data: (b) during one synoptic period of 12 hours, (c) for case 1 (March 11–20, 1993), and (d) for case 2 (March 16 to April 16, 1996).

Unlike other SAR data assimilation systems under development [*Hasselmann et al.*, 1996], we make no attempt to correct the wind fields locally near the SAR observation points. This is mainly because the temporal and spatial distribution of ERS wave mode data is too sparse to maintain wind corrections in the region associated with the storm track, and the impact of locally correcting the wind is expected to be minimal. One might expect that this will limit the lifetime of the corrections to the wave field, since the (possibly) inconsistent wind field would damp them out. However, even though SAR can detect some wind-field-driven wave components, particularly if they are range traveling, it primarily picks up low-frequency swell components, which are decoupled from the wind field. Eventually, it should be possible to use the swell corrections to adjust the wind at an earlier time in the simulation, but it will be necessary to use continuous (time-dependent) insertion methods to accomplish this. Owing to the scarcity of SAR wave data the corrections to the wind field will be most effective after being assimilated into an atmospheric model. We therefore believe that local wind corrections would have little or no effect on the demonstration of the utility of SAR data.

Table 2. Summary of Experimental Data Sets

	Model Input Data		Verification Data		
Case Study	CMC Forecast Winds	ERS-1 SAR Wave Mode	Buoys	ERS-1 Altimeter	ERS-1 SAR Wave Mode
1	yes	FDC	yes	FDC	FDC
2	yes	FDP	no	FDP	FDP

CMC, Canadian Meteorological Center; FDP, fast delivery product; FDC, fast delivery copy.

3. Data and Test Method

The system has been tested on two cases, representative of both a storm situation and a case of moderate sea state and wind conditions. The data available for the study consist of

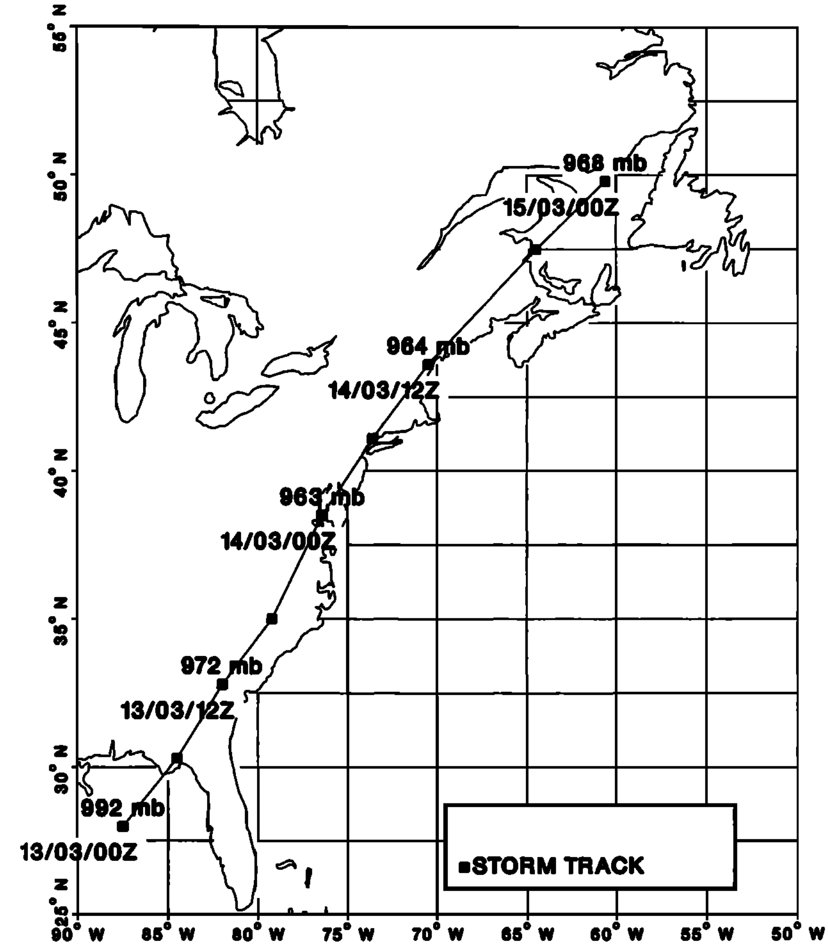

Figure 2. Track of the Storm of the Century, March 11–20, 1993.

model input data (wind fields for driving the model, and ERS SAR wave mode data for assimilation into the model) and verification data (ERS altimeter data (significant wave height), nondirectional wave buoy data, and inverted ERS SAR data not used in the assimilation.

The cases we have considered are listed in Table 1, details of the different data sets are shown in Table 2, and buoy locations and coverage of the satellite data for a typical 12-hour synoptic period are shown in Figure 1 along with the total coverage for the two cases. Case 1 is a particularly intense storm, referred to as the "Storm of the Century," which produced measured significant wave heights of 16.3 m south of Nova Scotia. The track of the storm is shown in Figure 2. Although the center of the storm remained inland, it was sufficiently close to the coast that very intense winds were maintained in the eastern half of the storm over the Atlantic. By 1800 UTC on March 13 a southeasterly flow of 45 knots (22.5 m s^{-1}) had developed over a large area south of 37°N. Six hours later, winds east of the storm center were reported as high as 60 knots (30 m s^{-1}), and 50-knot (25 m s^{-1}) southwesterly winds were reported behind the cold front south of the storm. As the storm moved northeastward, an intense southerly low level jet (60 knots reported) developed south of Nova Scotia and persisted for at least 12 hours. The wind sea developed in response to this jet later was supported by seas developed by an equally strong west-southwesterly flow, which followed the cold front as it swept eastward across the ocean south of Nova Scotia. It is the interaction of these wave systems that likely led to the reported maximum significant wave height at 0000 UTC on March 15. In general, the maximum significant wave heights were in the cold air closer to the coast, located generally well south of the storm center but following its track northeastward. The maxima were in excess of 14 m from 0000 UTC on March 14 until 1200 UTC on March 15. By March 16 the low had reached Iceland, producing an elongated area of westerly (eastward moving) high seas south of the storm from east of Newfoundland to south of Iceland. Seas had subsided over the western Atlantic by this time as a high-pressure area moved offshore.

In order to compare and contrast our results from a storm situation, we chose a contiguous month of data to use as a second case for assessing the assimilation method. This period, a late winter–early spring case, does not contain any major storms but represents sea sate conditions closer to normal for this time of year. The highest significant wave heights in this period were in the 8-m range.

3.1. Independent (Control) Data Sets

In this study, we have used altimeter, buoy, and SAR data for verification. The altimeter data, while offering only a bulk measurement of the sea state in the form of a significant wave height, offer the advantage of large spatial coverage and provide enough data to perform comparisons with model results in a significant sense. The altimeter data used in this study are summarized in Table 2. For case 1 we obtained 1106 observa-

Table 3. Buoy Station Information

	Station	Name	Depth, m	Latitude, °N	Longitude, °E
1	44005	Gulf of Maine	202	42.60	−68.60
2	44025	Long Island	···	40.30	−73.20
3	44004	Hotel	3231	38.50	−70.70
4	44141	Laurentian Fan	4500	42.07	−56.15
5	44139	Banquereau	1100	44.32	−57.35
6	44138	SW Grand Banks	1500	44.23	−53.35
7	44137	Scotian Shelf	4500	41.20	−61.13

Numbers in left column correspond to labels in Figure 1a.

tions that match a model counterpart value, and for case 2 we obtained 1289 observations. The altimeter data were processed as follows.

3.1.1. Averaging. The original altimeter data are sampled at approximately 0.06°, while the modeled data are represented on a 1° × 1° grid. For analyses involving comparisons of wave heights from the altimeter and the model, we computed an average wave height for every 1° of the orbit latitude along the track. Groups with fewer than 7 points were rejected before averaging, which removed most outliers.

3.1.2. Ice point removal. The altimeter data were provided with standard deviation estimates for wave height. Data with a standard deviation larger than 2 m were rejected before further use, as this is commonly used as an indicator for presence of ice [*Breivik and Reistad*, 1992].

Significant wave height data collected by seven nondirectional, 6-m NOMAD buoys were available only for case 1 (March 1993). The buoy locations are shown in Figure 1a, with details in Table 3.

3.2. Model Runs

In the present study, the WAM was driven in both hindcast and forecast modes by 10-m level winds obtained from the regional finite element (RFE) weather prediction model of the Canadian Meteorological Center (CMC) [*Mailhot et al.*, 1995]. The RFE model grid is a variable resolution grid with a central window of uniform resolution covering the region including the continental United States, Canada, and the Canadian Atlantic. The RFE model was run twice daily at 0000 UTC and 1200 UTC and generated forecast winds at 3-hourly intervals valid up to 48 hours, which were then interpolated onto the WAM grid.

In the hindcast mode, WAM was run using the first 12 hours (fields at 0, 3, 6, and 9 hours, referred to as 0h, 3h, 6h and 9h) of winds from each wind file. The 0h fields are analysis winds, while the 3h to 9h fields are forecasts. Two types of runs were done: baseline runs, with no assimilation, and assimilation runs, where for each 3-hour time step, SAR data were ingested, inverted, and assimilated. In order to perform comparisons between the model and the observations and to analyze the results for determining the impact of assimilating the SAR data, the model fields of wave height, period, and direction were stored for each time step. The inverted SAR spectra were also stored, along with the corresponding wave parameters calculated from these spectra.

In forecast mode the model was set up to run in a similar fashion. However, after each 12-hour assimilation period, forecast winds for the following 48 hours, again at 3-hour intervals, were used to produce a wave forecast. Thus forecast runs use forecast wind time series to drive the wave model. A new series was initiated every 12 hours through the period of each case. Again, these runs were conducted as baseline and assimilation runs. For the baseline runs there was no assimilation at all. For the assimilation runs, assimilation was done up to the 0h time of the forecast, as would be the case in operational forecasting.

For the detailed comparison of model results and observations from the satellite and wave buoys, the model data from grid points surrounding each observation location were extracted, and a bilinear interpolation was used to obtain a model

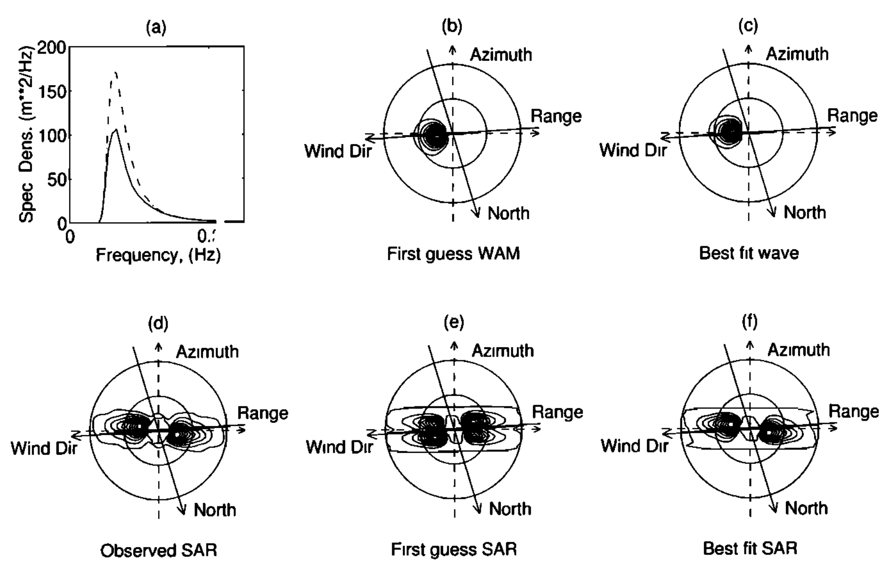

Figure 3. Example of inversion results for a single wave system. First guess and best fit frequency spectra (Figure 3a) are marked with the continuous and dot-dashed lines, respectively. Significant wave heights are 8.82 m for the modeled spectrum (Figure 3b) and 10.50 m for the inverted spectrum (Figure 3c). SAR image spectra are shown for the observed (Figure 3d), first-guess (Figure 3e), and best fit (Figure 3f) spectra. The radii of the outer and inner circles represent wave numbers corresponding to 100 m and 200 m wavelength, respectively.

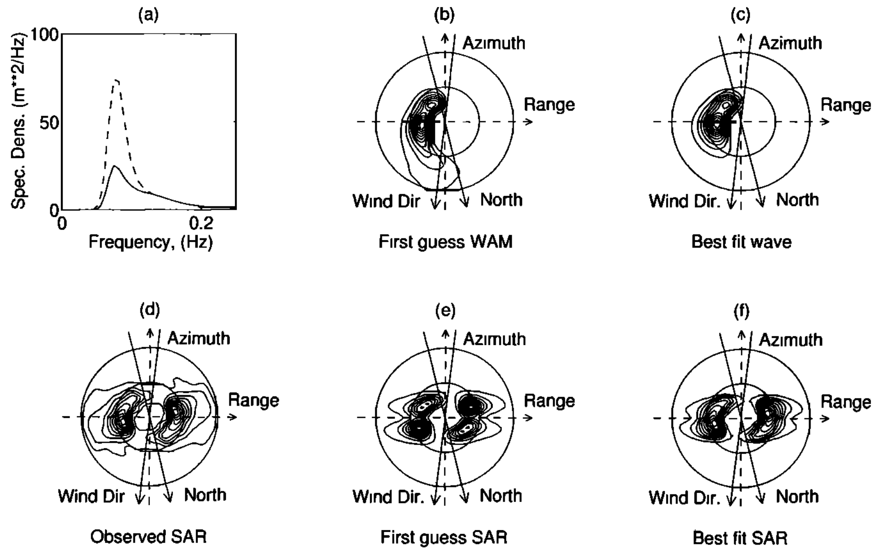

Figure 4. Same as Figure 3, but for two wave systems. Significant wave heights are 4.97 m for the modeled spectrum and 7.05 m for the inverted spectrum.

counterpart for each observation. This was done for the model time steps immediately before and after each observation. The model counterparts were then interpolated in time to match the time of the observation.

4. Results

The data sets and test methods described above were designed to allow us to determine the impact of the SAR data on wave analyses and forecasts from WAM. To assess the impact, we have compared the summary wave parameters from the different runs in different combinations. The statistics used in the comparison are defined in the appendix. The results of the comparisons are presented and discussed in this section, beginning with a discussion of the performance of the inversion algorithm and followed by an assessment of impacts on both hindcast and forecast runs compared to independent data. The verification was limited to comparisons of summary parameters because no directional spectral observations were available and because it is the summary wave parameters that were assimilated. Throughout this section, the run without assimilation is referred to as the "baseline run" and the runs with assimilation are called "assimilation runs."

4.1. Inversion

Examples of the inversion, for one and two wave systems are shown in Figures 3 and 4, respectively. Spectra are given in the azimuth and range coordinate system. True north and the corresponding wind velocity are also indicated. Wind direction is shown using the oceanographic convention, (i.e., "going to"). The first-guess and best fit SAR spectra are created by mapping the first-guess WAM and best fit wave spectra, respectively. Figure 3 shows that the inversion procedure leads to a spectral estimate with a slight directional change. The inversion also results in a larger significant wave height and a slight increase in the peak period. The result is seen to be closer to the corresponding wind direction. This case represents an almost range-traveling wave system. Thus nonlinear effects are small. However, the relatively broad wave spectrum with a single peak traveling in the range direction is often mapped into a double-peak SAR image spectrum on account of too small values of the RAR transfer function relative to the velocity bunching component [e.g., *Brüning et al.*, 1990]. The velocity-bunching mechanism vanishes in the range directions and rapidly resumes its large value on both sides of this direction. This leads to a deep, nonphysical trough in the spectrum. The calculated SAR spectrum was significantly modified in this case, compared with the first-guess SAR spectrum, changing from a split peak spectrum to a spectrum in which the peaks around the range wave number axis are joined together. After the inversion the simulated and observed SAR spectra are in much better agreement, with a pattern correlation coefficient increasing from 82.4% for the first guess to 99.4% for the best fit.

Figure 4 exhibits a case with two dominant wave modes. The inverted SAR spectrum shows a very large difference in wave energy (it actually doubles the wave height). Also, we observe that the relative peak strength changes. Here the pattern correlation coefficient increased from 89.6% to 95.7%.

Table 4 documents the overall inversion success rate, which is about 10% higher for the storm case than for case 2. This result is expected in the sense that the average wave height, and therefore the average signal strength in the SAR data is higher for the storm case. This in turn means that fewer spectra are likely to fail to invert because of low signal-to-noise ratio.

In general, we have found that the mean values of the significant wave height extracted from ERS-1 SAR wave mode spectra tend to exceed wave heights calculated by WAM by

Table 4. Number and Percent of Inverted SAR Image Spectra

Case	Total	Number Inverted	Percent Inverted	Percent Rejected
1	714	548	76.8	23.2
2	3504	2423	69.15	30.85

Table 5. Comparison of WAM Model Versus SAR-Based Estimates of Wave Height, Period and Direction for Case 1 (548 Samples) and Case 2 (2423 Samples)

	H_S, m		$\langle T \rangle$, s		$\langle k \rangle$, m^{-1}		$\langle$dir$\rangle$, deg	
	Case 1	Case 2	Case 1	Case 2	Case 1	Case 2	Case 1	Case 2
Mean (WAM)	4.09	2.88	9.24	8.27	0.05	0.06	140.86	152.13
Bias	0.43	0.38	0.28	0.31	−0.004	−0.005	−2.38	−4.59
Std	1.00	0.73	0.87	0.77	0.01	0.01	46.23	47.82
SI_D, %	25.36	6.70	9.27	9.84	18.59	19.67	33.12	31.24
Slope	1.10	1.13	1.03	1.02	0.93	0.92	0.98	1.001
Correlation, %	97.66	98.15	99.58	99.61	98.49	98.56	95.86	96.25

Notation is defined in the appendix. Cor, correlation.

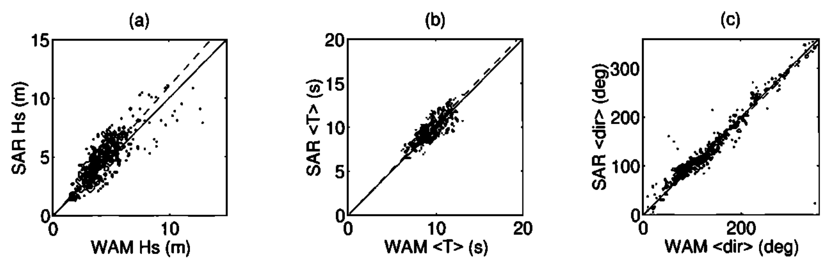

Figure 5. Scatter diagrams of the ERS-1 SAR based wave parameter estimates versus WAM based wave parameter estimates for case 1: (a) H_S, (b) average period, and (c) vector mean direction.

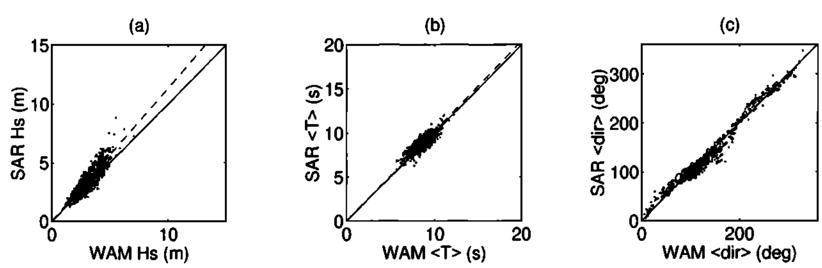

Figure 6. Same as Figure 5 but for case 2: (a) H_S, (b) average period, and (c) vector mean direction.

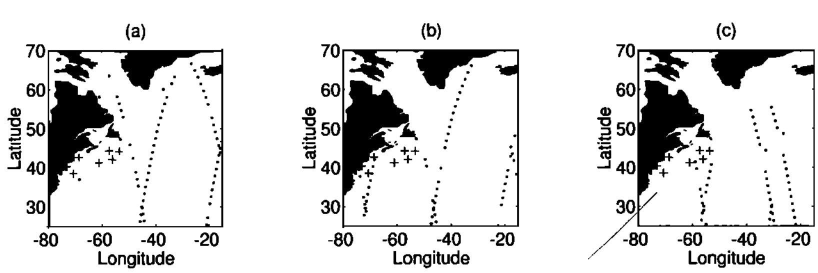

Figure 7. Coverage of assimilated SAR data in relation to buoys for case 1: (a) March 11, (b) March 14, and (c) March 16. Each panel shows 24-hour coverage.

approximately 10–12% (Table 5, Figure 5, and Figure 6). The bias is positive and larger for higher wave energies. This may be caused by a deficiency in the wind field driving WAM or by too small a value of the real aperture radar transfer function. A similar but negative bias, about 8%, was observed for the mean wave number. These results agree well with monthly statistics published by *Brüning and Hasselmann* [1993]. Figures 5 and 6 also show a comparison of wave directions. We observe that the predominant wave direction is within 50°–100°.

4.2. Hindcast Comparison With Buoy and Altimeter Data

In order to assess the impact of SAR data assimilation throughout the Storm of the Century, we compared model output with buoy observations. The results, however, are dependent on the buoy locations. The available buoy data locations are along the western fringe of the North Atlantic and are windward of most of the satellite observations. Therefore most of the wave systems and associated corrections arising from data assimilation propagate away from the buoy locations. The measurable impact is directly related to the region of influence and the spreading function applied. It is also very closely related to the spatial and temporal coverage of the SAR observations. In Figure 7 we show three examples of the 24-hour satellite coverage for March 11, 14, and 16, 1993. In Figures 8 and 9 we show time series comparing wave parameters from the model with buoy observations in the Gulf of Maine and off Long Island. The results are typical of all the buoy results and show that there is little difference in the two model runs, baseline and assimilation, early in the period but greater impact later on, coinciding with satellite passes closer to the buoy locations. We also see that the assimilation of SAR data results in a reduced overall difference between the model and the buoy observations. The improvement is most pronounced during periods of decaying waves. Table 6 shows a summary of the impact of the assimilation for each of the buoys, in terms of the changes in scatter index and correlation between buoy significant wave height and period and model significant wave height and period. Results are averaged over the 9-day period of case 1 and are based on about 183 observations for each buoy. Both the sample sizes and the observed changes are small. The overall scatter index is reduced by 0.3% and 1.55%, and the correlation is increased by 0.2% and 0.26% for the significant wave height and for the mean period, respectively. The impact on wave period is slightly greater than the impact on H_s. A typical example comparing wave height and period for one of the buoys on the Scotian Shelf is shown in Figure 10. The small effect of the assimilation is consistent with the fact that the buoys were very seldom within the influence region of ERS-1 data.

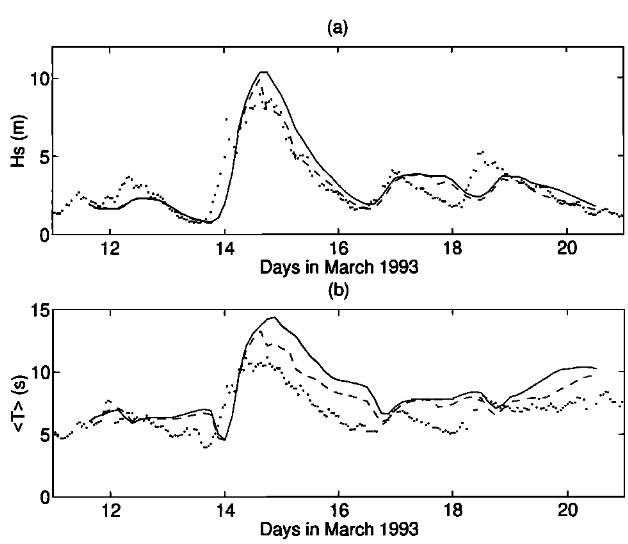

Figure 8. Comparison of hindcast series of (a) wave height and (b) mean period for buoy 44005 in the Gulf of Maine (case 1). Modeled wave parameters with and without assimilation are indicated by dashed and solid lines, respectively. Dots represent buoy observations.

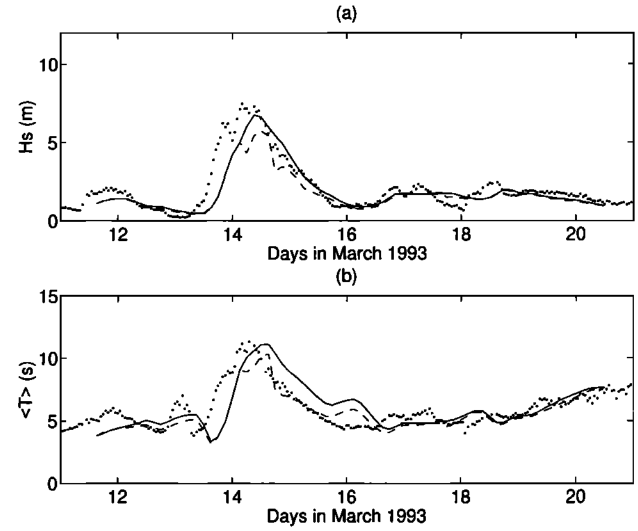

Figure 9. Same as Figure 8, but for buoy 44025 (Long Island).

In order to further understand the effect of assimilating SAR data in the case of the Storm of the Century, we measured the impact against observations from the ERS altimeter. The comparisons were made both in terms of summary statistics for all the data and in terms of individual satellite passes. In Figure 11a we show a selected satellite pass, which coincides with the storm area. The effect of assimilating the SAR observations for this pass, presented in Figure 11b (dashed line),

Table 6. Change in Scatter Index and Correlation Coefficient Between Buoy Significant Wave Height and Period and WAM/AWAM Model Significant Wave Height and Period, Due to SAR Data Assimilation

		H_S, m		$\langle T \rangle$, s	
Station	N	ΔSI_D, %	ΔCor_D, %	SI_D, %	ΔCor_D, %
44005	187	−2.46	0.23	−3.13	0.28
44025	185	3.53	0.72	−2.83	0.52
44004	182	−2.18	1.08	−1.91	0.64
44141	180	0.82	−0.24	−0.29	−0.05
44139	185	1.59	−0.22	−3.36	0.34
44138	179	−4.00	2.21	−3.02	0.83
44137	184	2.95	−0.18	−1.40	0.03
All buoys	1282	−0.30	0.21	−1.55	0.26

N is number of observations.

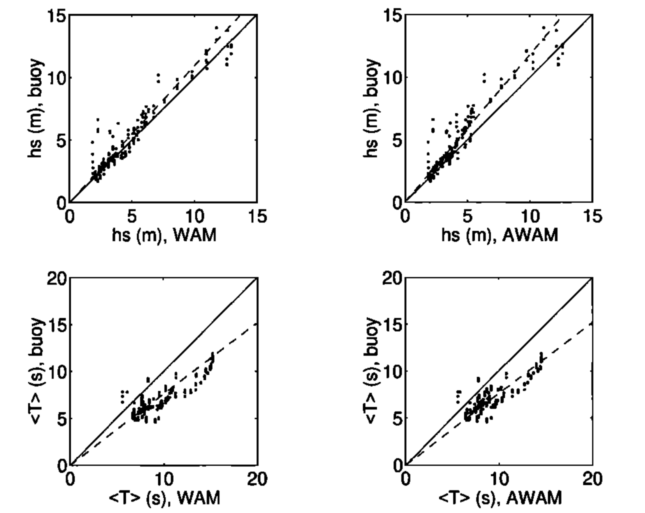

Figure 10. Comparison of buoy and model hindcast (top) wave heights and (bottom) mean periods for Scotian Shelf (buoy 44137), including (left) baseline run results and (right) assimilation run results. The dashed line is a least squares regression fit to the data points.

shows an improvement over the baseline case (solid line). In this case, the scatter index is decreased from 21.33% for the baseline run to 16.03% for the assimilation run, while the correlation coefficient is increased from 98.42% (baseline) to 99.02% (assimilation). The altimeter data show a dip in wave height between 38° and 40° along the track, which apparently was not resolved in the model. This feature is actually seen on several passes in the vicinity and is therefore not simply an artifact in the data. A glance at the analysis maps for the time of these altimeter measurements suggests that the dip in the significant wave height is related to a trough and associated wind shift from west to NW. The gradient in this area was also slackening with time. The feature was apparently not resolved in the modeled wave field. Even though the dip at the northern end of the track is not reproduced, the overall fit is better than that for the run without assimilation.

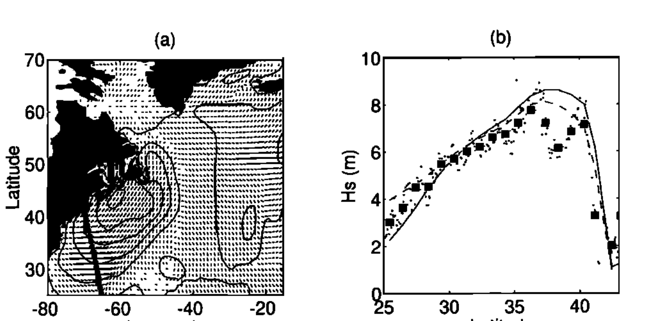

Figure 11. Comparison of altimeter and WAM significant wave heights along a specific satellite track for March 15, 0300 UTC. (a) Map showing contours of significant wave height and vector wave direction. Dots indicate location of averaged altimeter observations. (b) Significant wave height as a function of the latitude along the satellite track, for baseline run (solid line) and assimilation run (dashed line). Altimeter data averaged over a distance of 1° are indicated by squares. Maximum model H_S = 12.7 m.

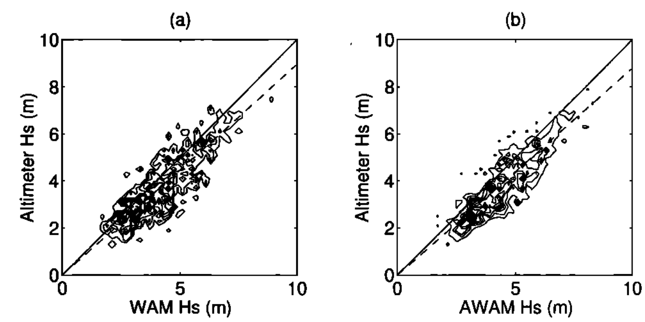

Figure 12. Scatter plots of WAM H_S versus ERS-1 altimeter wave heights for (a) the baseline run and (b) the assimilation run, for case 1. All hindcast series data are included. The dashed line is a least squares regression fit to the plotted data.

Our summary comparison of model results and altimeter data is shown in Figures 12 and 13 for the hindcast runs. The accompanying collocation statistics are given in Table 7. In both case 1 and case 2 we observe a clear tendency for the model to produce higher wave heights than the ERS-1 altimeter observes. In the storm case (see Table 7, case 1) the scatter index and correlation are slightly improved as a result of assimilation. An opposite tendency is observed for case 2. However, both cases have slopes that are farther from the ideal slope of 1 than the baseline run WAM result. Thus the overall trend of the assimilation has been to decrease the level of agreement between the altimeter and the model. This is in agreement with recently published results for the ERS-1 altimeter [e.g., *Breivik and Reistad*, 1992; P. A. E. M. Janssen, personal communication, 1996] which show that the ERS-1 altimeter systematically underestimates significant wave heights as compared with wave model results. Assimilation of SAR data augments this effect, as the SAR-enhanced wave spectra tend to overestimate the wave energy as compared with the model [*Brüning and Hasselmann*, 1993].

4.3. Forecast Comparisons

In the forecast assimilation runs, data were assimilated for a 12-hour period, and then a forecast was run for 48 hours. This was repeated for each 12-hour period for case 1 and case 2. In Figure 14 we show the root-mean-square of the difference and the bias between the baseline and assimilation runs for wave height, period, and direction. As we expected, the impact of

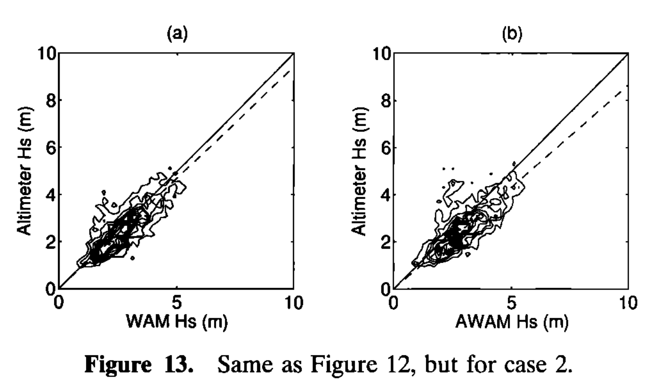

Figure 13. Same as Figure 12, but for case 2.

assimilating the SAR based corrections decays over time. This decay is more rapid for the storm situation in case 1 than in the more moderate conditions of case 2. In both cases the impact lasts for more than 36 hours into the forecast.

4.3.1. Comparison with altimeter. The results of intercomparison of significant wave heights measured by the ERS-1 altimeter and predicted by the wave model with and without SAR wave data assimilation are shown in Figure 15 for case 1 (1103 samples) and case 2 (3313 samples). The results include the scatter index and the correlation for both the analysis and the forecast. The results illustrate a slight but persistent improvement of the forecast result. The effect is stronger for the storm case, where the scatter is reduced by 1.6% and the correlation is increased by 0.2%, for the first 12 hours of forecast.

4.3.2. Comparison with SAR. To strengthen our verification of the assimilation results, we have also compared forecast model output with SAR observations not used in the assimilation up to that point in time. The results of this comparison show that the assimilation of SAR data improves the agreement between the data sets. In order to perform the comparisons, a model counterpart to each SAR observation was derived by bilinear interpolation of model data to the observation time and locations. The statistics of model results against the inverted but not yet assimilated wave data were averaged over three separate forecast ranges, 3–12 hours, 15–24 hours, and 27–36 hours. The comparison was made between the model with and without SAR data assimilation. The results are summarized in Table 8 and as a function of forecast time in Figure 16. We obtain a reduction in the scatter index of over 3% in wave height at the start of the forecast, which diminishes to less than 1% after 36 hours. The same trend is seen in wave period and mean direction, although with a little more variation in the case of wave direction. Figure 16 also shows that wave period is affected more in the storm case than in the moderate case. The opposite is seen to be the case for wave direction.

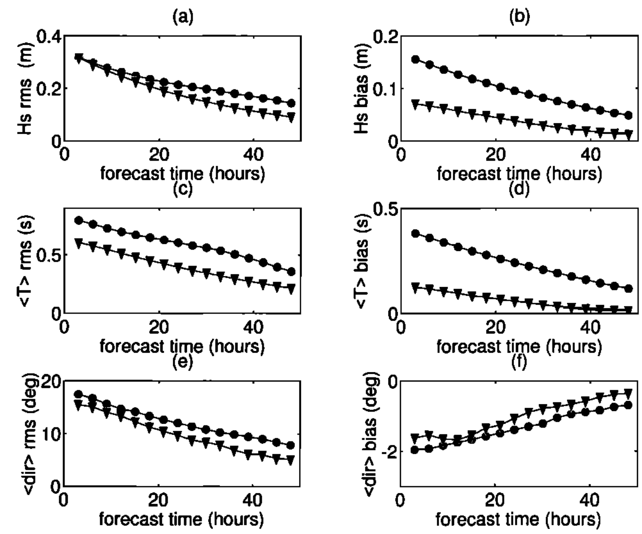

Figure 14. Plots of (left) root-mean-square difference and (right) mean difference between forecast wave parameters run from initial conditions with and without assimilation, as a function of projection time, for cases 1 (triangles) and 2 (circles). Results are given for (a, b) significant wave height, (c, d) average period, and (e, f) vector mean direction.

5. Discussion and Conclusions

We have built and tested an assimilation system for SAR wave data from ERS-1. The methodology, which treats both the inversion and the assimilation components separately, has been adapted from existing techniques. The system was embedded in a copy of the Canadian operational version of the WAM model, which runs over a regional domain covering most of the North Atlantic. We have demonstrated that the system can function reliably by running it on a storm event, and through 1 month of wave analyses and forecasts.

In addition to evaluating the assimilation performance in terms of the rate of successful inversion and assimilation, we have also compared both hindcasts and forecasts from the wave model with independent wave observations to determine the impact of the assimilation. In the verification, we used independent control data from the ERS-1 altimeter and non-

Table 7. Comparison of Significant Wave Heights With and Without Assimilation, Between Altimeter Measurements and Model Hindcast Results, for Case 1 and Case 2

	Case 1 (1103 Samples)		Case 2 (3313 Samples)	
	WAM	AWAM	WAM	AWAM
Mean (WAM)	4.32	4.45	2.68	2.94
Bias	−0.49	−0.62	−0.15	−0.41
Std	0.95	0.89	0.71	0.76
SI_D, %	23.26	21.52	27.40	27.95
Slope	0.89	0.88	0.94	0.87
Cor, %	97.74	97.90	96.87	96.79

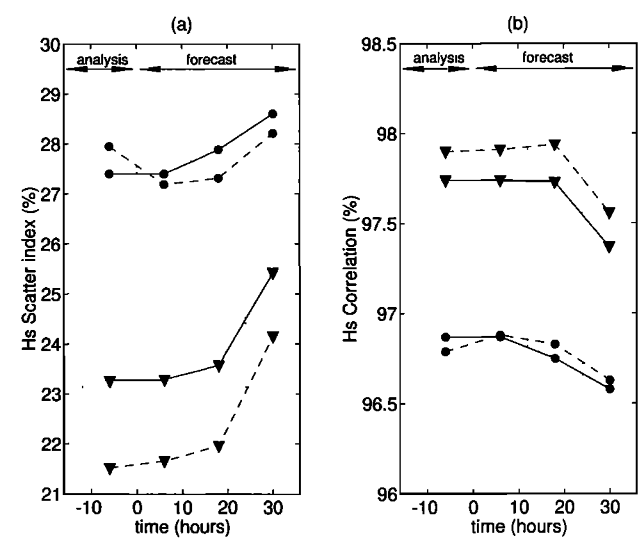

Figure 15. (a) Scatter index and (b) correlation with respect to altimeter H_S, as a function of projection time for case 1 (triangles, 1106 samples) and case 2 (circles, 1289 samples). Each data point represents results based on 12 hours of analysis or forecast. Results of the forecast following the baseline and assimilation runs are represented by solid and dashed lines, respectively.

Table 8. Statistical Comparison of First 12 Hour Forecast Results, Run From the Initial State With and Without Assimilation, Against Inverted but Not Yet Assimilated SAR Observations for Case 1 and Case 2

	Case 1 (376 Samples)		Case 2 (1717 Samples)	
	WAM	AWAM	WAM	AWAM
		H_S, *m*		
Mean (WAM)	4.49	4.64	2.88	3.11
Bias	0.44	0.39	0.63	0.39
Std	1.35	1.21	0.87	0.80
SI_D, %	28.95	25.77	27.39	24.21
Slope	1.05	1.03	1.23	1.15
Cor, %	96.35	97.12	97.26	97.82
		$\langle T \rangle$, *s*		
Mean (WAM)	10.51	10.77	8.99	9.52
Bias	−0.76	−1.02	−0.24	−0.77
Std	1.25	0.96	1.03	0.99
SI_D, %	12.32	9.33	11.58	10.81
Slope	0.92	0.90	0.97	0.99
Cor, %	99.29	99.59	99.35	99.46
		$\langle dir \rangle$, *deg*		
Mean (WAM)	141.59	137.60	153.3	137.60
Bias	−3.75	0.24	−8.63	−1.68
Std	42.91	40.28	55.98	42.97
SI_D, %	30.72	29.25	37.58	29.53
Slope	0.97	1.00	0.96	1.00
Cor, %	96.41	96.71	94.48	96.61

directional wave buoys. Owing partly to the lack of available independent two dimensional spectral wave observations, and also to the fact that the assimilation focuses on three summary parameters of the wave spectrum, the evaluation concentrated on the same parameters: significant wave height, average period, and wave direction. Since we could not obtain independent wave direction information, we also used not-yet-assimilated SAR data as another source of validation data, taking into consideration that the use of SAR data in the assimilation makes this a less independent data source.

Our comparison of the SAR wave data with the model wave parameters revealed that the SAR tends to give higher wave heights and longer periods than WAM and that the difference in wave height increases with higher sea states. This is in agreement with other published results.

When averaged over all the available data for a period of several days or more, the impact of the assimilation of SAR wave data was always small in magnitude. However, our comparisons with independent observations indicate that the impact was usually positive, that is, the average difference, the standard difference and the scatter index between the model and observed wave parameters usually were reduced slightly by the assimilation, while the correlation with independent observations increased slightly. There was one notable instance where a small negative impact was indicated, for the hindcast comparison with altimeter data for case 2, where both the bias and standard difference were increased by the assimilation.

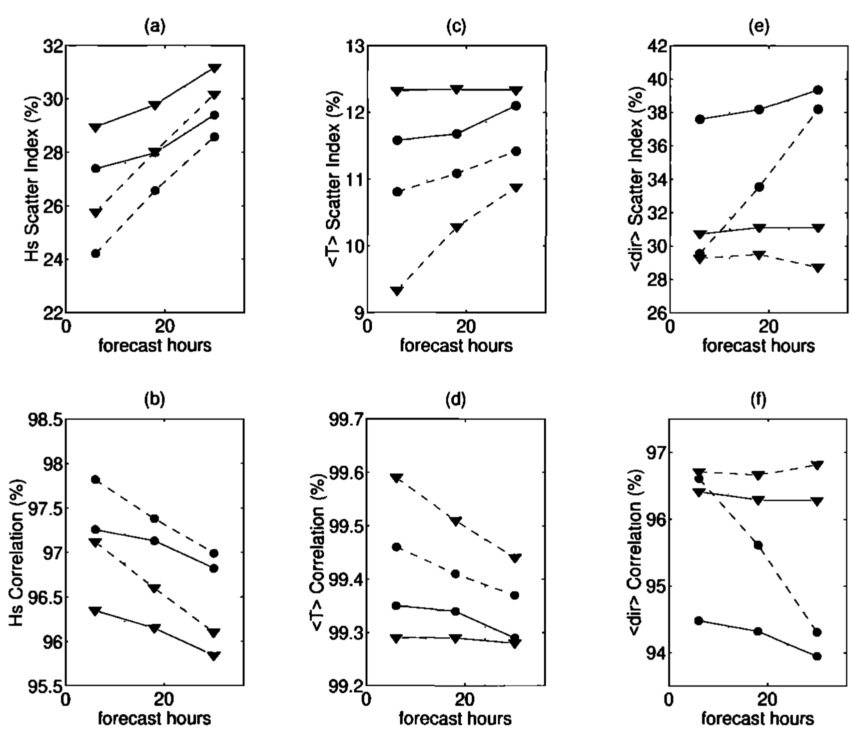

Figure 16. Scatter index and correlation with respect to wave parameters estimated from not-yet-assimilated SAR data, as a function of projection time for case 1 (triangles, 376 samples) and case 2 (circles, 749 samples). Results of the forecast following the baseline and assimilation runs are represented by solid line and dashed lines, respectively. Results are given for (a, b) significant wave height, (c, d) average period, and (e, f) vector mean direction.

The increase in negative bias in the altimeter comparisons, which also occurred for case 1, is attributed to the effect of systematic underestimating of wave heights by the ERS-1 altimeter, combined with the tendency of the SAR observations to overestimate the wave heights. We also note that the negative impact for the case 2 hindcast was reversed to a small positive impact for the forecast.

We attribute the small overall impact partly to the relative scarcity of the SAR data points compared with the number of model grid points. For the buoy data we also attribute the small overall impact to the scarcity of collocations of SAR data with the buoy observations and to the fact that the buoy observation locations tended to be upstream of the main wave propagation direction. Evaluation of the results of a single satellite pass indicated a locally larger positive impact with respect to buoy data when a near collocation occurred. The impact was most noticeable for the decaying stage of the waves and for wave period.

Our assessment of the persistence of the corrections indicated that the impact of assimilation decays with time but lasts for at least 36 hours into the forecast. This was also noted from comparisons of model results with the independent data. The corrections are relatively long lasting despite the fact that no attempt was made to adjust the wind field to agree with the modified wave field. This is consistent with the fact that corrections induced by SAR wave data mostly alter the low-frequency swell, for which the wind has little effect.

While the amount of wave data has increased dramatically to the point where routine wave data assimilation can now be considered worthwhile, data are still relatively scarce compared with what would be needed to have a really large impact on the model. The model estimates the spectrum at 2318 points over the North Atlantic, while in a 3-hour assimilation period, as many as 50 data points might be available. On average, the influence cannot be very large with that coverage rate. In fact, where there is particular interest, for example, in a storm situation, one has to be lucky to have a satellite overpass at the location and time of the storm.

Therefore, on the basis of the present results, we do not have enough evidence to conclude categorically that SAR data assimilation leads to improvement of wave analysis and forecast from WAM. Further study is needed on larger sample of collocated data. In particular, unbiased altimeter data would be helpful as an independent data source, especially if from the same satellite as SAR data. Directional buoy data will be useful for evaluation of the full spectrum. While additional validation data are needed, the inversion and assimilation methodology could also be improved in many ways. First, improvements can be made to the data quality control to lower the number of unsuccessful inversions and to help filter out non-wave field signals in the data. Second, the method of spreading corrections is very simple. The knowledge that the wave field is more highly correlated in the wave propagation direction can be built into the system through an anisotropic spreading weight function. However, it should also be feasible to move to a full optimum interpolation method, by obtaining the necessary error statistics for model and data. With the availability of increasingly large archives of higher quality wave observations, the necessary data are now becoming available. In the long run, the methodology can be optimized by using a full three-dimensional variational approach, but this will require dedication of greater amounts of computer power than is currently possible in operations.

Ultimately, the use of continuous insertion methods such as four-dimensional variational techniques will allow data from all sources to be blended with wave and atmospheric models to provide an optimal and consistent analysis of both waves and marine surface winds. For the future, we can hope that the availability of additional satellites (ERS-2, RADARSAT, and ENVISAT, for example) will result in an increase in data available to wave-modeling operations. Such an increase, along with a concurrent increase in the optimal use of the data in wave analysis and forecasting, will result in steady increases in accuracy of wave analyses and forecasts in the future.

Appendix: Statistical Parameters

Using S, f, θ, and x to refer to a spectrum, wave frequency, wave direction, and observed or modeled parameter, statistical parameters used in this paper are defined as follows.

Mean

$$\langle x \rangle = \frac{1}{N} \sum_{n=1}^{N} x_n \tag{A1}$$

Spectral mean

$$\langle x \rangle_S = \frac{\sum_{i,j} x(f_i, \theta_j) S^{\mathrm{WAM}}(f_i, \theta_j) \Delta f_i \Delta \theta_j}{\langle E \rangle_S} \tag{A2}$$

Mean energy

$$\langle E \rangle_S = \sum_{i,j} S^{\mathrm{WAM}}(f_i, \theta_j) \Delta f_i \Delta \theta_j \tag{A3}$$

Significant wave height

$$H_s = 4 \sqrt{\langle E \rangle_S} \tag{A4}$$

Mean period

$$\langle T \rangle_S \equiv \langle 1/f \rangle_S \tag{A5}$$

Vector mean direction

$$\langle \mathrm{dir} \rangle_S = \tan^{-1} \frac{\langle \sin(\theta) \rangle_S}{\langle \cos(\theta) \rangle_S} \tag{A6}$$

Mean wavelength

$$\langle k \rangle_S = \frac{1}{g} \left(\frac{2\pi}{\langle T \rangle_S} \right)^2 \tag{A7}$$

Standard deviation

$$\mathrm{std} = \sqrt{\langle (x - \langle x \rangle)^2 \rangle} \tag{A8}$$

$$\mathrm{Bias} = \langle x - x_{\mathrm{WAM}} \rangle \tag{A9}$$

Root mean square of the difference

$$\mathrm{rms} = \sqrt{\langle (x - x_{\mathrm{WAM}})^2 \rangle} \tag{A10}$$

Standard deviation of the difference

$$\mathrm{std}_D = \sqrt{\langle (x - x_{\mathrm{WAM}} - \mathrm{bias})^2 \rangle} \tag{A11}$$

Scatter index

$$\mathrm{SI} = \frac{\mathrm{std}}{\langle x \rangle} 100\% \tag{A12}$$

Scatter index of the difference

$$\mathrm{Si}_D = \frac{\mathrm{std}_D}{\sqrt{\langle x \rangle \langle x_{\mathrm{WAM}} \rangle}} 100\% \tag{A13}$$

Symmetric regression (slope) coefficient

$$(\bar{c}) = \sqrt{\frac{\langle x^2 \rangle}{\langle x_{\mathrm{WAM}}^2 \rangle}} = \frac{\mathrm{rms}}{\mathrm{rms}_{\mathrm{WAM}}} \tag{A14}$$

Symmetric correlation coefficient

$$\mathrm{Cor} = \frac{\langle x \, x_{\mathrm{WAM}} \rangle}{\sqrt{\langle x^2 \rangle \langle x_{\mathrm{WAM}}^2 \rangle}} \tag{A15}$$

Pattern correlation coefficient

$$K = \frac{\langle S_{\mathrm{SAR}}^{\mathrm{obs}} S_{\mathrm{WAM}}^{\mathrm{sim}} \rangle}{\sqrt{\langle (S_{\mathrm{SAR}}^{\mathrm{obs}})^2 \rangle \langle (S_{\mathrm{WAM}}^{\mathrm{sim}})^2 \rangle}} \tag{A16}$$

Acknowledgments. This work was carried out with funding from the Radar Data Development Program, Canada Centre for Remote Sensing, Environment Canada, and Panel for Energy Research and Development. The WAM model and algorithms for spectral mode separation and cross-assignment of corresponding wave systems were supplied by Susanne Hasselmann at the Max-Planck-Institut für Meteorologie.

References

Alpers, W., Monte Carlo simulations for studying the relationship between ocean wave and synthetic aperture radar image spectra, *J. Geophys. Res.*, *88*(C3), 1745–1759, 1983.

Alpers, W. R., and C. Bruning, On the relative importance of motion-related contributions to the SAR imaging mechanism of ocean surface waves, *IEEE Trans. Geosci. Remote Sens.*, *GE-24*, 873–885, 1986.

Bauer, E., S. Hasselmann, and K. Hasselmann, Validation and assimilation of Seasat altimeter wave heights using the WAM wave model, *J. Geophys. Res.*, *97*(C8), 12,671–12,682, 1992.

Bauer, E., S. Hasselmann, and C. Brüning, Application of wave spectra retrieved from ERS-1 SAR wave mode spectra in a wind- and wave data assimilation system, in *Proceedings, International Geoscience and Remote Sensing Symposium (IGARSS'95)*, pp. 1643–1646, IEEE, Piscataway, N. J., 1995.

Bao, M., C. Brüning, and W. Alpers, A generalized nonlinear integral transform and its application to ERS-1 SAR ocean wave imaging, in *Proceedings Second ERS-1 Symposium, Eur. Space Agency Spec. Publ., ESA SP-361*, 219–224, 1994.

Breivik, L. A., and M. Reistad, Use of ERS-1 altimeter wave products at DNMI—Evaluation of wave heights and wind speeds—Assimilation in a numerical wave model, *DNMI Report*, 23 pp., Det Norske Meteorol. Inst., Oslo, 1992.

Brooker, G., UWA processing algorithm description, *ESA Doc. ER-Tn-ESA-GS-0341*, Issue 1.1, Eur. Space Agency, Paris, Jan. 19, 1994.

Bruning, C., and S. Hasselmann, Global statistics of integrated ocean wave parameters extracted from ERS-1 SAR wave mode image spectra, in *Proceedings, International Geoscience and Remote Sensing Symposium (IGARSS093)*, Tokyo, pp. 351–353, IEEE, Piscataway, N. J., 1993.

Brüning, C., W. Alpers, and K. Hasselmann, Monte-Carlo simulations of the nonlinear imaging of a two dimensional surface wave field by a synthetic aperture radar, *Int. J. Remote Sens.*, *11*, 1695–1727, 1990.

Brüning, C., S. Hasselmann, K. Hasselmann, S. Lehner, and T. Gerling, On the extraction of ocean wave spectra from ERS-1 SAR wave mode image spectra, in *Proceedings of the First ERS-1 Symposium, Eur. Space Agency Spec. Publ., ESA-SP 359*, 747–752, 1993.

Brüning, C., S. Hasselmann, K. Hasselmann, S. Lehner, and T. Gerling, First evaluation of ERS-1 synthetic aperture radar wave mode data, *Global Atmos. Ocean Syst.*, *2*, 61–98, 1994a.

Brüning, C., R. Schmidt, and W. Alpers, Estimation of the ocean wave–radar modulation transfer function from synthetic aperture radar imagery, *J. Geophys. Res.*, *99*(C5), 9803–9815, 1994b.

Cressman, G. P., An operational objective analysis system, *Mon. Weather Rev.*, *87*, 367–374, 1959.

de las Heras, M. M., and P. A. E. M. Janssen, Data assimilation with a coupled wind-wave model, *J. Geophys. Res.*, *97*(C12), 20,261–20,270, 1992.

Engen, G., H. Johnsen, H. E. Krogstad, and S. F. Barstow, Directional wave spectra by inversion of ERS-1 synthetic aperture radar ocean imagery, *IEEE Trans. Geosci. Remote Sens.*, *32*, 340–352, 1994.

Francis, P. E., and P. P. Stratton, Some experiments to investigate the assimilation of Seasat altimeter wave height data into a global wave model, *Q. J. R. Meteorol. Soc.*, *116*, 1225–1251, 1990.

Gandin, L. S., *Objective Analysis of Meteorological Fields*, 242 pp., Isr. Program for Sci. Transl., Jerusalem, 1963.

Gerling, T. W., Partitioning sequences and arrays of directional wave spectra into component wave systems, *J. Atmos. Oceanic Technol.*, *9*, 444–458, 1992.

Graber, H., V. Cardone, R. Jensen, S. Hasselmann, H. L. Tolman, and L. Cavaleri, The accuracy of wind field description, in *Dynamics and Modeling of Ocean Waves*, Chap. IV.3.2, pp. 285–293, Cambridge Univ. Press, New York, 1994.

Hasselmann, K., and W. Alpers, The response of synthetic aperture radar to ocean surface waves, in *Wave Dynamics and Radio Probing of the Ocean Surface*, edited by D. M. Phillips and K. Hasselmann, pp. 393–400, Plenum, New York, 1986.

Hasselmann, K., and S. Hasselmann, On the nonlinear mapping of an ocean wave spectrum into a synthetic aperture radar image spectrum and its inversion, *J. Geophys. Res.*, *96*, 10,713–10,729, 1991.

Hasselmann, K., R. K. Raney, W. J. Plant, W. Alpers, R. A. Shuchman, D. R. Lyzenga, C. L. Rufenach, and M. J. Tucker, Theory of synthetic aperture radar ocean imaging: A MARSEN view, *J. Geophys. Res.*, *90*(C3), 4659–4686, 1985.

Hasselmann, S., C. Brüning, and P. Lionello, Towards a generalized optimal interpolation method for the assimilation of ERS-1 SAR retrieved wave spectra in a wave model, in *Proceedings Second ERS-1 Symposium, Eur. Space Agency Spec. Publ., ESA SP-361*, 21–25, 1994.

Hasselmann, S., C. Brüning, K. Hasselmann, and P. Heimbach, An improved algorithm for the retrieval of ocean wave spectra from synthetic aperture radar image spectra, *J. Geophys. Res.*, *101*(C7), 16,615–16,629, 1996.

Jacobsen, S., and K. A. Høgda, Estimation of the real aperture radar modulation transfer function directly from synthetic aperture radar ocean wave image spectra without a priori knowledge of the ocean wave height spectrum, *J. Geophys. Res.*, *99*(C7), 14,291–14,302, 1994.

Jain, A., SAR imaging of ocean waves, Theory, *IEEE J. Oceanic Eng.*, *OE-6*, 130–139, 1981.

Janssen, P. A. E. M., Quasi-linear theory of wind-wave generation applied to wave forecasting, *J. Phys. Oceanogr.*, *21*, 1631–1642, 1991.

Komen, G. J., L. Cavaleri, M. Donelan, K. Hasselmann, S. Hasselmann, and P. A. E. M. Janssen, *Dynamics and Modeling of Ocean Waves*, Cambridge University Press, New York, 1994.

Krogstad, H. E., A simple derivation of Hasselmann's nonlinear ocean–synthetic aperture radar transform, *J. Geophys. Res.*, *97*(C2), 2421–2425, 1992.

Krogstad, H. E., O. Samset, and P. W. Vachon, Generalization of the non-linear ocean-SAR transform and a simplified SAR inversion algorithm, *Atmos. Ocean*, *32*, 61–82, 1994.

Lasnier, P., H. Hajii, S. Loeul, D. Bonicel, and B. Chapron, Use of SAR-wave mode, altimeter and wind scatterometer data in operational wave forecasting system, in *Proceedings Second ERS-1 Symposium, Eur. Space Agency Spec. Publ., ESA SP-361*, 21–25, 1994.

Lionello, P., H. Gunther, and P. A. E. M. Janssen, Assimilation of altimeter data in a global third-generation wave model, *J. Geophys. Res.*, *97*(C9), 14,453–14,474, 1992.

Lionello, P., H. Günther, and B. Hansen, A sequential assimilation scheme applied to global wave analysis and prediction, *J. Mar. Syst.*, *6*, 87–107, 1995.

Mailhot, J., R. Sarrazin, B. Bilodeau, N. Brunet, A. Methot, G. Pellerin, C. Chouinard, L. Garand, C. Girard, and R. Hogue, Changes to the Canadian regional forecast system: Description and evaluation of the 50 km version, *Atmos. Ocean*, *33*, 55–80, 1995.

Raney, R. K., and R. T. Lowry, Oceanic wave imagery and wave spectra distortions by synthetic aperture radar, paper presented at 12th International Symposium on Remote Sensing of the Environment, Environ. Res. Inst. of Mich., Manila, April 20–26, 1978.

Talagrand, O., and P. Courtier, Variational assimilation of meteorological observations with the adjoint vorticity equation, I, Theory, *Q. J. R. Meteorol. Soc.*, *113*, 1311–1328, 1987.

Vachon, P. W., R. K. Raney, and W. J. Emery, A simulation for spaceborne SAR imagery of a distributed, moving scene, *IEEE Trans. Geosci. Remote Sens.*, *27*, 67–78, 1989.

Vachon, P. W., R. B. Olsen, H. E. Krogstad, and A. K. Liu, Airborne synthetic aperture radar observations and simulations for waves in ice, *J. Geophys. Res.*, *98*(C9), 16,411–16,425, 1993.

Vachon, P. W., H. E. Krogstad, and J. S. Paterson, Airborne and spaceborne synthetic aperture radar observations of ocean waves, *Atmos. Ocean*, *32*, 83–112, 1994.

Wave Model Development and Implementation (WAMDI) Group (S. Hasselmann et al.), The WAM model—A third generation ocean wave prediction model, *J. Phys. Oceanogr.*, *18*, 1775–1810, 1988.

Zambreski, L., A verification study of the global WAM model, December 1987–November 1988, *ECMWF Tech. Rep. 63*, Eur. Cent. for Medium-Range Weather Forecasts, Reading, England, 1989.

E. M. Dunlap and S. De Margerie, ASA Consulting Ltd., 1888 Brunswick Street, Suite 400, Halifax, Nova Scotia, Canada B3J 3J8. (e-mail: edunlap@esa.ca)

R. B. Olsen, Satlantic, Inc., Richmond Terminal, Pier 9, 3295 Barrington Street, Halifax, Nova Scotia, Canada B3K 5X8. (e-mail: richard@satlantic.com)

R. Lalbeharry and L. Wilson, Atmospheric Environment Service, Environment Canada, 2121 Trans-Canada Highway, Suite 500, Dorval, Quebec, Canada H9P 1J3.

(Received January 3, 1997; revised August 27, 1997; accepted September 8, 1997.)